A MATHEMATICAL ANALYSIS OF RECONSTRUCTION ARTIFACTS IN RADAR LIMITED DATA TOMOGRAPHY*

ELENA MARTINEZ†
PROJECT ADVISOR: ERIC TODD QUINTO, PH.D.‡

Abstract. In the study of tomography, there are often missing data values. This leads artifacts to present themselves in data reconstructions. We investigate this problem in a bistatic radar system that has a radio transmitter in a fixed location and a receiver flying around the transmitter in a circular path. Our data is collected by integrating over all ellipses in a given space that have the transmitter and receiver as foci. We reconstruct this numerical data and analyze the artifacts that present themselves when we place objects within and outside of the receiver's path. Our research demonstrates how objects outside the receiver's path can create artifacts inside the receiver's path and vice versa. This shows an intrinsic limitation to a method that works well when the scanned region outside the receiver's path is clear.

Key words. radar, limited data tomography, reconstruction algorithms

AMS subject classifications. 44A12, 92C55, 65R32

1. Introduction.

Tomography is the mathematics, science, and engineering used to recover the interior structure of a nontransparent object using indirect data. Tomography imaging systems produce cross-sectional images that are used to find solutions to a wide range of problems in varying fields, such as the biosciences and aeronautics. For example, in the medical field, x-ray computed tomography (CT) produces cross-sectional images that are used to view the internal organs of a patient. With x-ray CT, an object is placed in a scanner and x-rays are taken over evenly distributed lines that pass through all parts of the object. We call such data complete tomographic data [17]. There are times, however, when we cannot acquire a complete data set due to either a limited view, limited angle, or lack of efficiency [3]. In many types of tomography, including x-ray tomography, photoacoustic tomography, and thermoacoustic tomography, data can only be obtained from a limited field of view. When we are missing data values, we call this data limited tomographic data [12]. Tomography with limited tomographic data is more challenging than with complete tomographic data because standard tomographic algorithms need to be adjusted in order to get accurate reconstructions [14, 15].

We focus specifically on limited tomographic data as it applies to radar. While radar was originally developed in order to determine the position of objects through echo-location, using radar for imaging has gained popularity, especially within the engineering community [19]. Radar-based imaging, however, faces challenges such as detecting microwave energy, transmitting microwave energy at high power, and interpreting and extracting information from received signals. While the first two problems have been addressed through hardware development, the third challenge is substantially a mathematical issue [2].

*This work was funded by the VERSE and VERSEIM-REU programs at Tufts University under NSF grant DMS 1712207 and NSF REU grant DMS 2050412.

†Department of Mathematics, Loyola Marymount University, Los Angeles, CA (emarti78@lion.lmu.edu).

‡Department of Mathematics, Tufts University, Medford, MA (todd.quinto@tufts.edu).

The images obtained from tomographic imaging systems are called reconstructions. Reconstructions generated from limited tomographic data often contain artifacts. Artifacts are additional singularities that are generated in a reconstruction and often superimpose reliable information. This is important because artifacts can create unwanted features in our image that may lead us to misinterpret data [10]. We focus on artifacts in reconstructions of a bistatic radar imaging system. In such systems, a transmitter and a receiver are in different locations. We simulate and reconstruct our receiver's data to address three objectives: (1) describing the artifacts we obtain when we place objects within the receiver's path using complete tomographic data, (2) describing the artifacts we obtain when we place objects outside of the receiver's path using complete tomographic data, and (3) describing the artifacts we obtain when the receiver does not complete its circular path, i.e. using limited tomographic data.

Our research looks at artifacts that result from placing a disk object within the receiver's circular path and artifacts that result from placing a disk object outside of the receiver's circular path. There is a lack of information regarding how objects outside a receiver's path affect the reconstruction of the area within the receiver's path. Our research addresses this gap. We demonstrate that there are limitations to this data acquisition method because artifacts can present themselves inside the receiver's path when the region outside the receiver's path is not clear.

This paper is organized as follows. In section 2, we describe how we generate the data. In section 3, we describe how we generate our reconstructions using a back-projection operator and second central difference model. We demonstrate and analyze our reconstruction images in section 4. Finally in section 5, we draw unifying conclusions based off our analysis of reconstructions and describe the next steps to be taken.

2. Data Generation. In our bistatic radar system, we have a receiver traveling along the unit circle and a transmitter at the origin. The data acquisition model that we study in this paper enables a transmitter to be a fixed object that is already in the region such as a radio or cell phone antenna and enables the receiver to be a small drone that can fly around a region undetected. When imaging an object, the waves from the transmitter are reflected off of the object and then travel to the receiver. As seen in Figure 1, the distance from the transmitter (T) to the object (O) is d_1 and the distance from the object to the receiver (R) is d_2. The major diameter of the resulting ellipse is represented by d. We measure the strength of the signal at the receiver against time using the formula $\frac{d_1+d_2}{c} = t$ where c is the speed of the waves. By the definition of an ellipse $d_1 + d_2 = d$. Therefore, at each time t, the receiver is measuring the integral of reflectivity for an ellipse that satisfies the equation $d = ct$ and the receiver and transmitter are the foci [16].

In this section, we define the integral over an ellipse with the characteristics illustrated in Figure 1. First, we parameterize our initial ellipse. Next, we introduce a rotation matrix that will give us the parameterization of each following ellipse based on time t. Then, we define our characteristic function. Upon solving for this function we calculate the line integral and implement a convolution to smooth our data. Finally, we describe a derivative method that sharpens the features of objects.

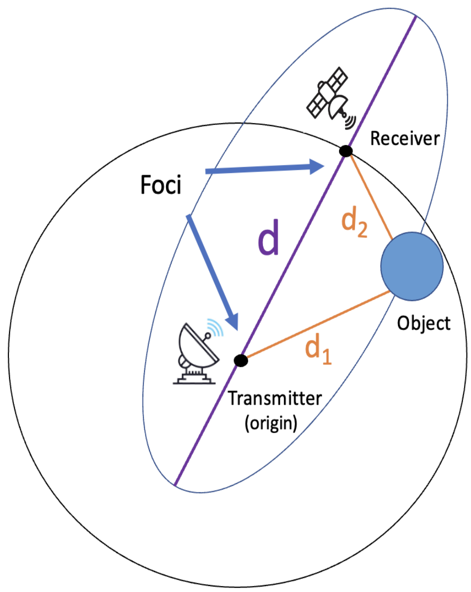

Fig. 1: Labeled bistatic radar system

This derivative method is inspired by Lambda Tomography [7, 6, 10].

2.1. Ellipse Parameterization. First, we need to parameterize our initial ellipse. Let s be the variable that parameterizes the ellipse. An ellipse centered at (x_0, y_0) can be parameterized using (2.1) where $d = 2a$ is the length of the major diameter and b is length of the minor axis.

$$\begin{cases} x(s) = x_0 + a(\cos(s)) \\ y(s) = y_0 + b(\sin(s)) \end{cases} \tag{2.1}$$

The foci of our initial ellipse are (0,0) and (1,0) and therefore this ellipse is centered at $(\frac{1}{2}, 0)$. Let c be the distance between the center and either focus. Using formula $b^2 = a^2 - c^2$, $c = \frac{1}{2}$ and $a = \frac{d}{2}$, we get $b = \frac{\sqrt{d^2-1}}{2}$. Therefore, our initial ellipse can be parameterized using (2.2).

$$\vec{\gamma}(s) = \begin{bmatrix} \frac{d\cos(s)+1}{2} \\ \frac{\sqrt{d^2-1}\sin(s)}{2} \end{bmatrix} \tag{2.2}$$

2.2. Rotation Matrix. Since our receiver is traveling along the unit circle, we use a rotation matrix to find the parameterization of each ellipse at parameter s. Let ϕ be the angle between the major diameter of an ellipse and the x-axis. $A(\phi) = \begin{bmatrix} \cos(\phi) & -\sin(\phi) \\ \sin(\phi) & \cos(\phi) \end{bmatrix}$ rotates an ellipse with major diameter d and foci (0,0) and (1,0) to the ellipse with foci (0,0) and $(\cos(\phi), \sin(\phi))$ and major diameter d. Since our receiver is traveling along the unit circle, to parameterize an ellipse at position $(\cos(\phi), \sin(\phi))$ we multiply $A(\phi)$ and (2.2). We get $\vec{\gamma}_\phi(s) = A(\phi)\vec{\gamma}(s)$ rewritten below.

$$\vec{\gamma}_\phi(s) = \begin{bmatrix} \frac{d\cos(\phi)\cos(s)+\cos(\phi)-\sqrt{d^2-1}\sin(\phi)\sin(s)}{2} \\ \frac{d\sin(\phi)\cos(s)+\sin(\phi)+\sqrt{d^2-1}\cos(\phi)\sin(s)}{2} \end{bmatrix} \tag{2.3}$$

2.3. Characteristic Function. The integral of reflectivity will depend on the object that we are imaging, so we must define a characteristic function based on the shape of that object. A characteristic function is chosen because it models a homogeneous object in a homogeneous field, i.e. a water tower in a desert. Since we are studying artifacts and visible features of objects, objects with simple shape are easier to analyze. Thus, we focus on reconstructing disks. The characteristic function of a disk with center (x_0, y_0) and radius r is given by (2.4).

$$g(x,y) = \begin{cases} 1, & \text{if } \sqrt{(x^2 - x_0^2) + (y^2 - y_0^2)} \leq r \\ 0, & \text{otherwise} \end{cases} \tag{2.4}$$

2.4. Line Integral. Lastly, in order to find the integral of reflectivity of an object over an ellipse, we calculate the line integral over each ellipse. s goes from 0 to 2π, so using the formula for a line integral we have

$$Rf(d,\phi) = \int_0^{2\pi} g\left(\vec{\gamma}_\phi(s)\right) ||\vec{\gamma}_\phi'(s)|| ds \tag{2.5}$$

After finding the derivative of $\vec{\gamma}(s)$ we get $\vec{\gamma}'(s) = \left(\frac{-d\sin(s)}{2}, \frac{\sqrt{d^2-1}\cos(s)}{2}\right)$ [5, 4]. Since $\vec{\gamma}_\phi(s) = A(\phi)\vec{\gamma}(s)$, and $A(\phi)$ is a rotation, $\vec{\gamma}_\phi(s)$ and $\vec{\gamma}(s)$ have the same norm. Similarly, $\vec{\gamma}'(s)$ and $\vec{\gamma}_\phi{}'(s)$ have the same norm. Thus, we can find the norm of $\vec{\gamma}'(s)$ using (2.6).

$$||\vec{\gamma}_\phi{}'(s)|| = ||\vec{\gamma}^{'}(s)|| = \frac{\sqrt{d^2 - \cos^2(s)}}{2} \tag{2.6}$$

By substituting equation (2.6) into equation (2.5), we obtain the final equation for finding the reflectivity of an object over an ellipse where $s \in [0, 2\pi]$. f is the characteristic function of the object we are imaging. Equation (2.7) represents this final equation.

$$Rf(d,\phi) = \int_0^{2\pi} g(\vec{\gamma}_\phi(s)) \frac{\sqrt{d^2 - \cos^2(s)}}{2} ds \tag{2.7}$$

We integrate over ellipses with foci at the origin and on the unit circle up to $d_{max} = 7$. These ellipses cover a $[-2, 2] \times [-2, 2]$ square. d is the major diameter of the ellipse and we need the whole ellipse to enclose the square $[-2, 2] \times [-2, 2]$. Any ellipse with foci at the origin and on the unit disk with $d_{max} = 7$ will enclose this square. We increment $d \in [1, d_{max}]$ using $\Delta_d = \frac{d_{max}-1}{k}$ where k is the number of points dividing $[1, d]$. For each d, we increment every ϕ within the interval $[0, 2\pi]$ using $\Delta\phi = \frac{2\pi}{l}$ where l is the number of points dividing $[0, \phi]$. We define d_i for $i = 0, 1, 2, ..., k-1$ as $d_i = 1 + i * \Delta_d$. We define ϕ_j for $j = 0,...,l-1$, as

$$\phi_j = \frac{2\pi j}{l} \tag{2.8}$$

Let $E(d,\phi)$ be the ellipse with foci (0,0) and $(\cos(\phi),\sin(\phi))$ and with major diameter d. We find $Rf(d,\phi)$ from $t\in[0,2\pi]$ using the trapezoidal rule, obtaining a specific intensity value for each $E(d_i,\phi_j)$. Our last step is to place each intensity value in a 2D array which we call ψ, where $\psi[i,j]=Rf(d_i,\phi_j)$. Using MATLAB, we programmed a function that incorporates all of these steps and outputs ψ. Algorithm 2.1 belows outlines this code. After generating ψ, we smooth our data using a convolution method. From here, we take the numerical second derivative in d of this smoothed data. Taking the derivative helps sharpen boundaries and rapid changes in values [7, 6, 10]. Using both the convolution and derivative methods allows us to better analyze artifacts that present themselves in our reconstructions.

Algorithm 2.1 Data Generation Algorithm

Input k = number of points to divide Δd
$\bar{x}$ = all the curves of integration that go through x $\in[-2,2]^2$
l= number of points to divide ϕ
n= number of points to divide $\bar{x}$
Δs= change in angle parameterizing the ellipse
Output ψ = 2D array with all the data values
$d_{max}=7$
$\Delta d=\frac{d_{max}-1}{k}$
$\Delta\phi=\frac{\phi_a-\phi_b}{l}$
for i in 0:k **do**
  $d=1+i*\Delta d$
  for j in 0:l **do**
    $\phi=j*\Delta\phi$
    $\vec{\gamma}_\phi=\begin{bmatrix}\frac{d\cos(\phi)\cos(s)+\cos(\phi)-\sqrt{d^2-1}\sin(\phi)\sin(s)}{2}\\ \frac{d\sin(\phi)\cos(s)+\sin(\phi)+\sqrt{d^2-1}\cos(\phi)\sin(s)}{2}\end{bmatrix}$
    characteristic = $(\sqrt{\vec{\gamma}_\phi[0]-x_0)^2+(\vec{\gamma}_\phi[1]-y_0)^2})$
    if characteristic $\le r$ **then**
      $f=1$
    else
      $f=0$
    end if
    $\Delta s=\frac{2\pi}{2n}$
    trapezoidal = 0
    for m = 0:n **do**
      s = m*Δs
      Rf = $f*\frac{\sqrt{d^2-\cos^2(s)}}{2}$
      trapezoidal + = Rf
    end for
  end for
  $\psi[i,j]$ = trapezoidal
end for
return ψ

2.5. Convolution Method. We want a general idea of relatively slow changes of values within our data set. We also want to pay little attention to oscillation between nearby data values. Using a convolution method for smoothing helps important patterns clearly stand out. We convovle our data with respect to d since the data are generally smoother in ϕ and thus convolution and smoothing are not needed.

Let ω_1 be our data after it has been smoothed using this convolution method. To produce ω_1, we convolve ψ in d. We want to find the weighted average at each $\psi[i,j]$. We fix ϕ_j and average values of $\psi(d_i,\phi_j)$ for nearby values of d. For the majority of our points, we use a five-point discrete convolution method that creates a symmetry around the point $\psi[i,j]$ while focusing on d_i. For our edge cases, however, we do not have five points to work with. Therefore, we use different formulas for the first two i values and the last two i values. For every entry in ψ, we fill ω_1 using Algorithm 2.2 below, where k and l are defined in subsection 2.4. For each $\psi[i,j]$ value, while the points immediately next to d_i hold significant weight, d_i holds the greatest weight.

2.6. Derivative Method. In addition to the convolution method, we take the second central difference in d to approximate the second derivative of our smoothed data. Let ω_2 be the final version of our data produced by implementing the derivative method. To obtain ω_2, we sharpen the smoothed ω_1 data. The second central difference approximates the second derivative according to the formula $f^{''}(x_i) \approx \frac{g(x_{i+1})-2g(x_i)+g(x_{i-1})}{h^2}$ where $h = x_i - x_{i-1}$ is the distance between neighboring x values in a discrete domain. For every entry in ω_1, we fill ω_2 using Algorithm 2.3 on the following page. As demonstrated by our first reconstructions in section 4, sharpening our data helps make artifacts in our reconstructions more identifiable. Thus ψ represents the original data, ω_1 represents the result of applying convolution to ψ, and ω_2 represents the result of applying the derivative method to ω_1.

Algorithm 2.2 Convolution Method

```
Input k, l as defined in Algorithm 2.1
Output ω1 = data smoothed using convolution
for i in 0:k do
for j in 0:l do
  if i=0 then
    ω1[i,j] = 3ψ[0,j]/6 + 2ψ[1,j]/6 + ψ[3,j]/6
  end if
  if i=1 then
    ω1[i,j] = 2ψ[0,j]/8 + 3ψ[1,j]/8 + 2ψ[2,j]/8 + ψ[3,j]/8
  end if
  if i=k then
    ω1[i,j] = ψ[k−2,j]/6 + 2ψ[k−1,j]/6 + 3ψ[k,j]/6
  end if
  if i=k-1 then
    ω1[i,j] = ψ[k−3,j]/8 + 2ψ[k−2,j]/8 + 3ψ[k−1,j]/8 + 2ψ[k,j]/8
  else
    ω1[i,j] = ψ[i−2,j]/9 + 2ψ[i−1,j]/9 + 3ψ[i,j]/9 + 2ψ[i+1,j]/9 + ψ[i+2,j]/9
  end if
 end for
end for
return ω1
```

Algorithm 2.3 Derivative Method

Input k, l as defined in Algorithm 2.1
Output ω_2 = data sharpened using second central difference
for i in 0:k **do**
for j in 0:l **do**
  if i=1 **then**
    $\omega_2[i,j] = \frac{\omega_1[0,j]-2\omega_1[1,j]+\omega_1[2,j]}{{\Delta_d}^2}$
  end if
  if i=k **then**
    $\omega_2[i,j] = \frac{\omega_1[k-2,j]-2\omega_1[k-1,j]+\omega_1[k,j]}{{\Delta_d}^2}$
  else
    $\omega_2[i,j] = \frac{\omega_1[i-1,j]-2\omega_1[i,j]+\omega_1[i+1,j]}{{\Delta_d}^2}$
  end if
end for
end for
return ω_2

3. Data Reconstruction.

After generating ω_2, we create reconstructions of disks with different radii and place them in various locations. We use both a back-projection dual operator and a linear interpolation method to create these reconstructions.

3.1. Back-projection.

For each $\bar{x} = (x_1, x_2)$, the backprojection operator integrates Rf (as described in (2.7)) over all ellipses $E(d, \phi)$ that contain $\bar{x}$. Therefore, given $\bar{x}$, for each $\phi \in [0, 2\pi]$, we find the value of d such that $\bar{x} \in E(d, \phi)$, and denote it by $d(\phi, \bar{x})$. As seen in Figure 2, we have one focus at the origin and another focus at $\bar{\phi} = (\cos(\phi), \sin(\phi))$. We also know that $d = d_1 + d_2$, as described in section 2. Therefore, we can find the value of d based on a given ϕ and $\bar{x}$ using equation (3.1).

$$d(\phi, \bar{x}) = ||\bar{x}|| + ||\bar{x} - \bar{\phi}|| \tag{3.1}$$

The back-projection operator evaluated at $\bar{x} = (x_1, x_2)$ averages the data over all the curves of integration that go through $\bar{x}$. It is defined by the equation (3.1) [13, 8] ([13] explains why interpolation is useful). (3.2) gives the analytic definition of R^* when evaluated on Rf.

$$R^*Rf = \int_0^{2\pi} Rf(d(\phi, \bar{x}), \phi) d\phi. \tag{3.2}$$

We increment $\bar{x} \in [-2, 2] \times [-2, 2]$, our area of interest, using $\Delta_{x_1} = \Delta_{x_2} = \frac{4}{n}$ where n is a selected number of points. For each $\bar{x}$ we increment ϕ using $\Delta_\phi = \frac{2\pi}{l}$, as defined in section 2. We store the increment count in variable p and substitute $\bar{x}$ and ϕ into equation (3.1) to find d. However, $d(\phi, \bar{x})$ might not be equal to d_i for any i. We will now find the closest d_i less than or equal to $d(\phi, \bar{x})$ to estimate $Rf(d(\phi, \bar{x}), \phi)$.

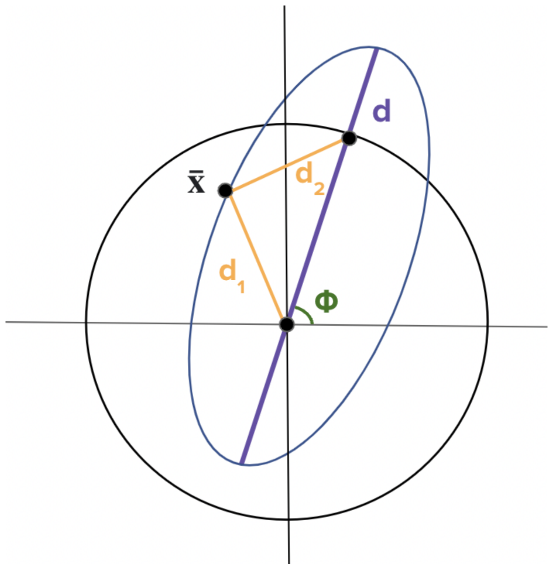

Fig. 2: E(d,ϕ) that passes through $\bar{x}$

To find this value, we must determine the correct i index. Let's assume our indices start at 0. Index i iterates through d values, so we are searching for value d_i. Since d_i is the largest value such that $d_i \leq d(\phi, \bar{x})$, we want i to be the largest integer such that $d_i = 1 + (d_{max} - 1)\frac{i}{n} \leq d(\phi, \bar{x})$. Solving for i gives us equation (3.3).

$$i = \left\lfloor \frac{(d-1)n}{d_{max} - 1} \right\rfloor \tag{3.3}$$

We also need to find the correct ϕ_j value. The value for j depends on the starting and ending angle for ϕ. If we have complete tomographic data then $\phi_a = 0$ and $\phi_b = 2\pi$. Our range for ϕ could be less than 2π if we have limited tomographic data. We solve for ϕ_j using (3.4).

$$\phi_j = \phi_a + \frac{(\phi_b - \phi_a)j}{l} \tag{3.4}$$

3.2. Interpolation. Linear interpolation is a method of curve fitting that estimates a function by fitting line segments between two data points. Now that we have i and j for each $\bar{x}$,ϕ pair, we can use the following interpolation formula, where z is the resulting data point [1].

$$z = \frac{(\omega_2[i+1, j] - \omega_2[i, j])(d - (1 + i\Delta d))}{\Delta d} + \omega_2[i, j] \tag{3.5}$$

Let τ be a matrix representing the reconstruction at the array points $\bar{x} = (x_1, x_2)$, where $\bar{x} \in [-2, 2] \times [-2, 2]$. We calculate $\tau = R^* \omega_2$ with the trapezoidal rule to numerically approximate $R * Rf$ as defined in equation (3.2). Each value of $Rf(d(\phi, \bar{x}), \phi)$ is found using equation (3.5). We plot τ using MATLAB's imagesc(C) function, where

C is a 2D array. This function displays the data in C as an image where each element of C specifies the color for one pixel of the image. The result is an $n_1 \times n_2$ grid of pixels where n_1 is the number of rows and n_2 is the number of columns in C [18].

4. Reconstructions. In this paper we focus on reconstructions over region $[-2, 2] \times [-2, 2]$ where the object of interest is a disk. We set the radii of the disks that we analyze to be $\frac{1}{4}$, $\frac{1}{2}$, or $\frac{3}{4}$. For all of our reconstructions, we let $k = 400$, $l = 400$, and $n = 400$. Therefore, $\Delta d = \frac{d_{max}-1}{k} = \frac{3}{200}$ and $\Delta\phi = \frac{\phi_a - \phi_b}{l} = \frac{\pi}{200}$. The x-axis of our images represents x_1 which we increment by $\Delta x_1 = \frac{2-(-2)}{400} = \frac{1}{100}$. The y-axis of our images represents x_2 which we increment by $\Delta x_2 = \frac{2-(-2)}{400} = \frac{1}{100}$.

In Figure 3a, we reconstruct a disk centered at the origin with a radius $r = \frac{1}{2}$. In this reconstruction, we use the convolution method to smooth our data, but we do not use the derivative method for sharpening. In Figure 3b, we reconstruct the same disk object centered at the origin with a radius of $\frac{1}{2}$, with data that has been sharpened by the derivative method. It is difficult to see the details of the reconstruction in Figure 3a. In Figure 3b, however, we see more detail and a clearer outline of the disk. We see that the boundary of the disk is well-reconstructed. This illustrates the importance of using a derivative method to sharpen boundaries and rapid changes in data values. Therefore, we focus on reconstructions that employ both the convolution and derivative method to produce our data and the following images reconstruct τ. In terms of artifacts, we have a circle artifact with a radius of 1.5. We also have an ellipse artifact tangent to the rightmost border of the outer-circle.

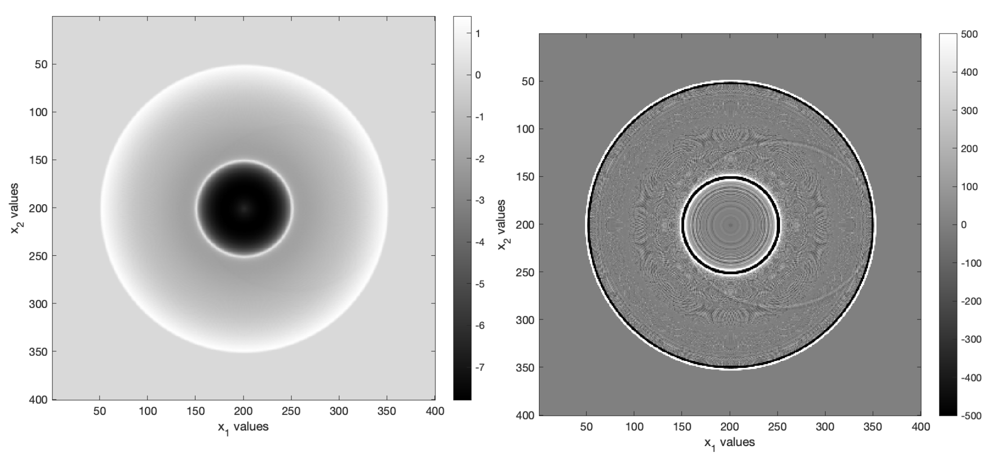

(a) reconstructed using data omitting the derivative method

(b) τ reconstruction.

Fig. 3: Disk at (0,0) with r = $\frac{1}{2}$

In Figure 4a, we reconstruct a disk centered at $(0, \frac{1}{10})$ with radius $r = \frac{1}{4}$. In Figure 4b, we also have a disk centered at $(0, \frac{1}{10})$ with a radius of $\frac{1}{4}$, but we also include a coloring for where the unit circle is using the color purple and a coloring for where the object should be located in the reconstruction using magenta. We use this same coloring for Figure 5b, Figure 6b, Figure 7b, Figure 8b, and Figure 9b.

Although the disk object is not centered at the origin, the origin is still within the disk. Similar to Figure 3b, Figure 4a and Figure 4b show that the disk's boundary is well-reconstructed, but we have a white ellipse with a major diameter on the x-axis. Also like Figure 3, we have a circle artifact with a radius of 1.5.

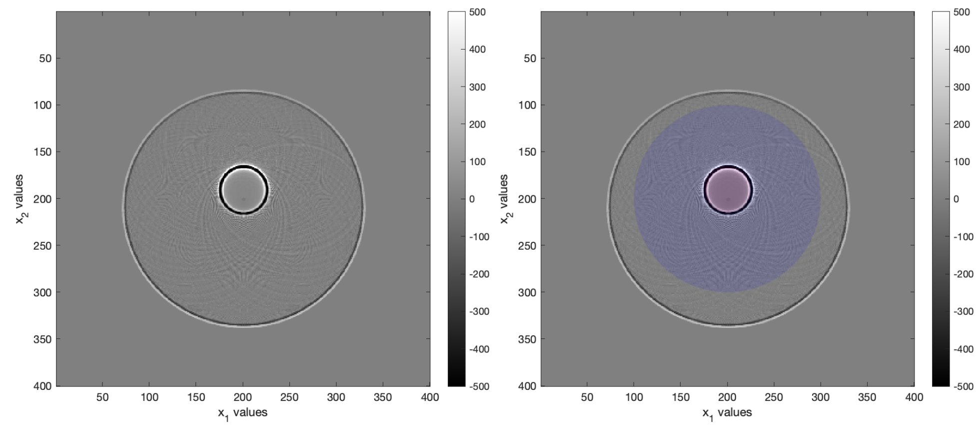

(a) τ reconstruction (b) Highlighted τ reconstruction

Fig. 4: Disk at $\left(0, \frac{1}{10}\right)$ with r $= \frac{1}{4}$

In Figure 5a and Figure 5b, we reconstruct a disk with center $(0,\, \frac{1}{2})$ and radius $r = \frac{1}{4}$. In these figures, we see that although the top border of the disk is reconstructed well, the bottom border of the disk is not clearly outlined. Instead, we have a v-shaped artifact that extends from the bottom border of the disk down towards the origin.

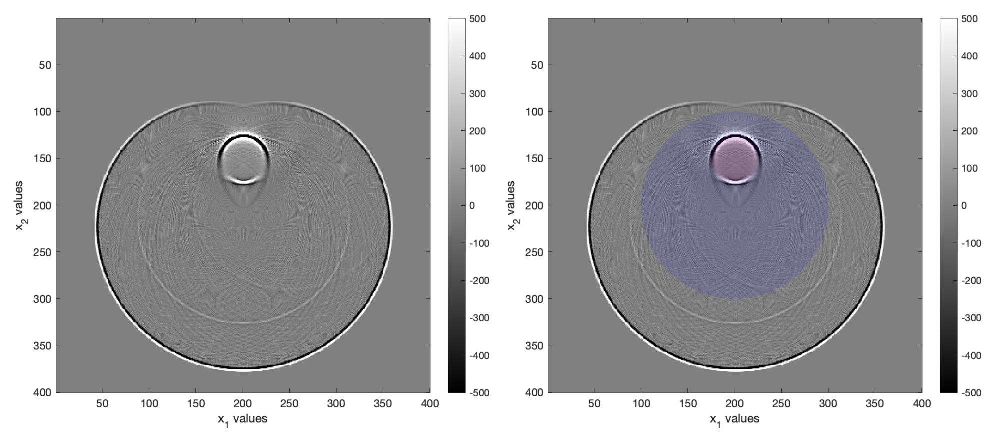

(a) τ reconstruction (b) Highlighted τ reconstruction

Fig. 5: Disk at $\left(0, \frac{1}{2}\right)$ with r $= \frac{1}{4}$

In Figure 6a and Figure 6b, we construct a disk that is centered at $\left(\frac{1}{2}, 0\right)$ with a radius $r = \frac{1}{2}$. By looking at Figure 6b, we see that this disk is tangent to the unit circle, which is represented in purple. We see that cardioid-shaped artifacts are starting to form on the right side of the outermost circle. These cardioid-shaped artifacts do not cross into the unit circle.

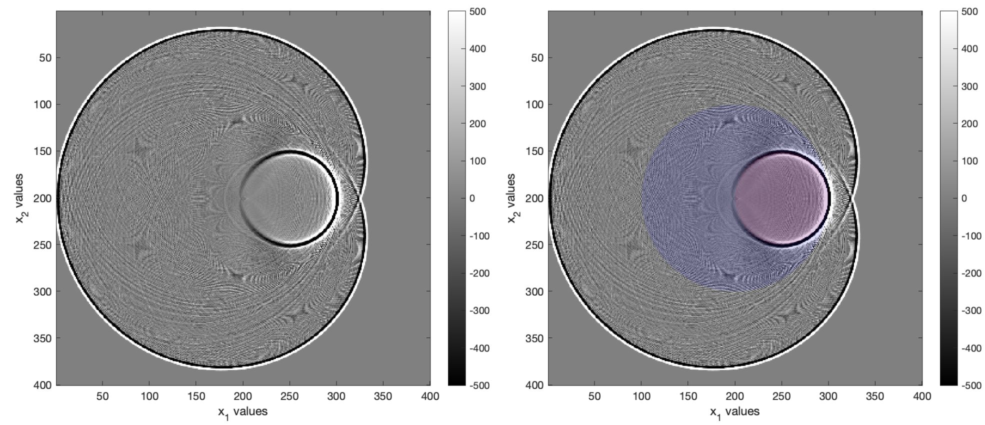

(a) τ reconstruction (b) Highlighted τ reconstruction

Fig. 6: Disk at $\left(\frac{1}{2}, 0\right)$ with r $= \frac{1}{2}$

In Figure 7a and Figure 7b, we reconstruct a disk centered at (1, 0) with radius $r = \frac{3}{4}$. In this case, we have a disk that is half inside and half outside of the unit circle. By looking at Figure 7a, we can clearly tell that the border of the disk is not reconstructed well. We also see cardioid-shaped artifacts forming both within and outside of the unit circle.

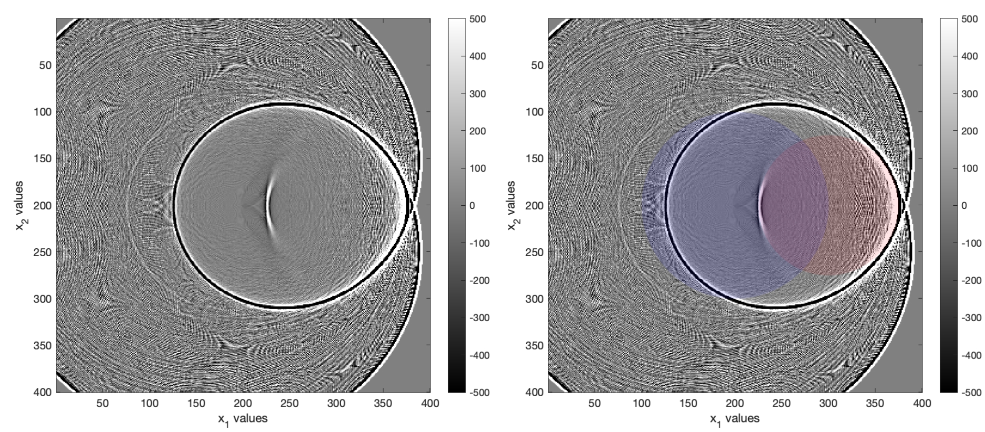

(a) τ reconstruction (b) Highlighted τ reconstruction

Fig. 7: Disk at (1, 0) with r $= \frac{3}{4}$

In Figure 8a and Figure 8b, we reconstruct a disk with center $\left(\frac{3}{2}, \frac{3}{2}\right)$ and $r = \frac{1}{2}$. Here, the object is entirely outside of the unit circle. The reconstructions produce the disk's right and left boundaries, but not the top or bottom. There are cardioid-shaped artifacts outside of the unit circle that cross into the unit circle. These cardioids are more noticeable than the cardioids in Figure 7a, Figure 7b, Figure 6a, and Figure 6b.

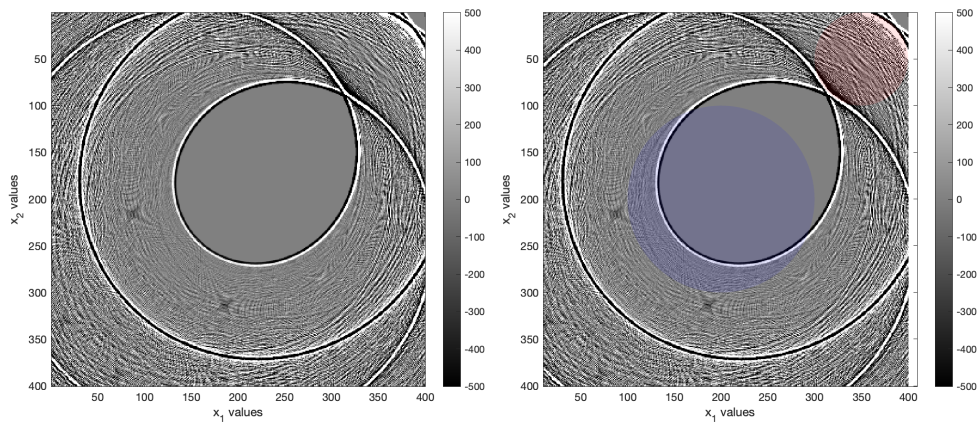

(a) τ reconstruction (b) Highlighted τ reconstruction

Fig. 8: Disk at $\left(\frac{3}{2}, \frac{3}{2}\right)$ with r $= \frac{1}{2}$

In Figure 9a and Figure 9b, we reconstruct a disk centered at (0,0) with $r = \frac{1}{2}$, and a limited interval for ϕ. We restrict ϕ to be within $[0, \pi]$ instead of $[0, 2\pi]$. In these figures, the top part of the disk is well-reconstructed, but the bottom extends out into a cardioid. There is a white ellipse at outermost circle's start, with a major diameter at $\phi = 0$, and at the outermost circle's end with major diameter $\phi = \pi$.

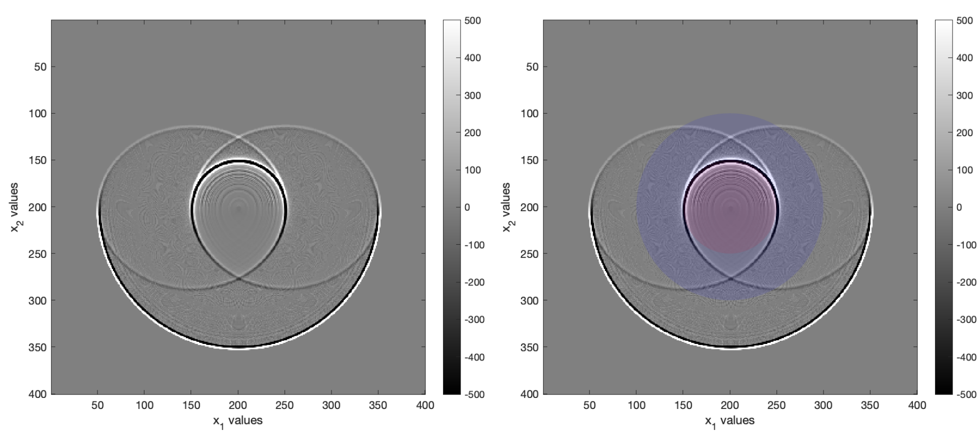

(a) τ reconstruction (b) Highlighted τ reconstruction

Fig. 9: Disk at (0,0) with r $= \frac{1}{2}$, $\phi \in [0, \pi]$

5. Conclusions. Figure 3a, Figure 3b, Figure 4a, and Figure 4b are reconstructions of disks that are inside the unit circle and contain the origin. Figure 5a and Figure 5b reconstruct a disk that is inside the unit circle but the disks do not contain the origin. Figure 6a and Figure 6b reconstruct a disk with a boundary that is tangent to the unit circle. Figure 7a and Figure 7b reconstruct a disk that is partially within and partially outside of the unit circle. Figure 8a and Figure 8b reconstruct a disk that is completely outside of the unit circle. Finally, Figure 9a and Figure 9b reconstruct a disk created from limited tomographic data. Based on these reconstructions as well as similar reconstructions, we see that

1. If an object is within the receiver's path (within the unit circle) and the origin is within the object, then the object's boundary will be will reconstructed. There will, however, be an artifact curve outside the unit circle and a white ellipse artifact with its major diameter on the x-axis.

2. If an object is within the receiver's path but the object does not contain the origin, then we have a v-shaped artifact stretching from the origin to the object.

3. If the object is partially within and partially outside of the receiver's path or if the object is tangent to the receiver's path, then we have the beginnings of cardioid-shaped artifacts.

4. If the object is completely outside of the receiver's path, then we have very obvious cardioid-shaped artifacts that appear both within and outside of the receiver's path.

5. If we have a limited interval for ϕ, meaning we cannot reconstruct the receiver's entire path, then our reconstructions have two white ellipses; one at ϕ_a and the other at ϕ_b.

Our next steps are to use microlocal analysis to determine whether the artifacts described in the five points above are numerical [9, 11]. We seek to determine what is causing the white circle to appear in reconstructions described in conclusions 1 and 5 and the cardioids described in conclusions 3 and 4. While we also worked with square-shaped and rectangle-shaped objects, we have yet to analyze these reconstructions. Our next steps involve drawing conclusions regarding reconstructions with rectangle-shaped and square-shaped objects and determining how our conclusions differ to the conclusions described above.

Acknowledgments. We would like to acknowledge the Tufts Visiting and Early Research Scholars' Experiences Program (VERSE), the Tufts VERSEIM REU program through NSF site REU grant DMS 2050412, Prof. Quinto's NSF grant DMS 1712207, and the Leadership Alliance for their support of our research.

REFERENCES

[1] M. R. A. Bacha, A. Oukebdane, and A. H. Belbachir, Implementation of the zero-padding interpolation technique to improve angular resolution of x-ray tomographic acquisition system, Pattern Recognition and Image Analysis, 26 (2016), pp. 817 – 823, https://doi.org/10.1134/S1054661816040143.

[2] M. Cheney and B. Borden, Problems in synthetic-aperture radar imaging, SIAM Journal on Matrix Analysis and Applications, 25 (2009), https://doi.org/10.1088/0266-5611/25/12/123005.

[3] J. K. Choi, B. Dong, and X. Zhang, Limited tomography reconstruction via tight frame and simultaneous sinogram extrapolation, SIAM Journal for Applied Mathematics, 75 (2015), pp. 703 – 725, https://doi.org/10.1137/140977709.

[4] A. Cormack, Representation of a function by its line integrals with some radiological applications ii, Journal of Applied Physics, 35 (1964), pp. 2908 – 2913, https://doi.org/10.1063/1.1713127.

[5] A. M. Cormack, Representation of a function by its line integrals with some radiological applications, Journal of Applied Physics, 34 (1963), pp. 2722 – 2727, https://doi.org/10.1063/1.1729798.

[6] A. Faridani, D. Finch, E. L. Ritman, and K. T. Smith, Local tomography, II, SIAM J. Appl. Math., 57 (1997), pp. 1095–1127.

[7] A. Faridani, E. L. Ritman, and K. T. Smith, Local tomography, SIAM J. Appl. Math., 52 (1992), pp. 459–484.

[8] J. A. Fessler, Statistical Image Reconstruction Methods for Transmission Tomography, SPIE Press, Bellingham, Washington USA, 2003.

[9] D. Finch, I. Lan, and G. Uhlmann, Microlocal analysis of restricted x-ray transform with sources on a curve, in Inside out, inverse problems and applications, MSRI Publications, vol. 47, Cambridge University Press, Cambridge, 2003, pp. 193 – 218.

[10] J. Frikel and E. T. Quinto, Artifacts in incomplete data tomography with applications to photoacoustic tomography and sonar, SIAM J. Appl. Math., 75 (2015), pp. 703–725, https://doi.org/10.1137/140977709.

[11] L. Hörmander, The analysis of linear partial differential operators. I. Classics in Mathematics, Springer, Berlin, 2003. Distribution theory and Fourier analysis, Reprint of the second (1990) edition.

[12] P. Kuchment and E. T. Quinto, Some problems of integral geometry arising in tomography, in The Universality of Radon Transform, Oxford University Press, London, 2003.

[13] B. Liu, G. Wang, E. L. Ritman, G. Cao, J. Lu, O. Zhou, L. Zeng, and H. Yu, Image reconstruction from limited angle projections collected by multisource interior x-ray imaging systems, Physics in Medicine and Biology, 56 (2011), pp. 6337 – 6357, https://doi.org/10.1088/0031-9155/56/19/012.

[14] F. Natterer, The Mathematics of Computerized Tomography, Classics in Mathematics, Society for Industrial and Applied Mathematics, New York, 2001.

[15] F. Natterer and F. Wübbeling, Mathematical Methods in Image Reconstruction, Monographs on Mathematical Modeling and Computation, Society for Industrial and Applied Mathematics, New York, 2001.

[16] S. J. Norton and M. Linzer, Ultrasonic reflectivity tomography; reconstruction with circular transducer arrays, Ultrason Imaging, 1 (1979), pp. 703 – 725, https://doi.org/10.1177/016173467900100205.

[17] E. T. Quinto, Artifacts and visible singularities in limited data x-ray tomography, Sensing and Imaging Journal, 18 (2017), https://doi.org/10.1007/s11220-017-0158-7.

[18] C. Solomon and T. Breckon, Fundamentals of Digital Image Processing: A Practical Approach with Examples in Matlab, Wiley-Blackwell, 2011.

[19] W. Waite, Historical development of imaging radar, geoscience applications of imaging radar systems, Remote Sensing of the Electro Magnetic Spectrum, 3 (1976), pp. 1 – 22.